Solar Energy 245 (2022) 353–364

Contents lists available at ScienceDirect

Solar Energy

journal homepage: www.elsevier.com/locate/solener

Electronic, structural, and optical properties of Cs_2SnGeX_6 (X = I, Br, Cl) and mixed halides for solar cell applications

D. Bharath Raja [a], R. Vidya [b,*], K. Shanmuga Sundaram [a]

[a] Department of Mechanical Engineering, College of Engineering, Anna University, Sardar Patel Road, Guindy, Chennai 600 025, India
[b] Department of Medical Physics, College of Engineering, Anna University, Sir. C.V. Raman Science Block, Sardar Patel Road, Guindy, Chennai 600 025, India

ARTICLE INFO

Keywords:
Solar cell
Perovskites
DFT method
Bandgap
Mixed-halides
Lone-pairs

ABSTRACT

The mixed metal-halide perovskites of the form ABX_3, (where, A is the organic or inorganic cation, B is the metal cation, and X is the halide anion) have a wide range of tunable structural and electronic properties leading to intense research over the past decade. This study reports the density functional theory calculations on the sn-Ge based perovskite Cs_2SnGeX_6 (where, X = I, Br, Cl), for determining the most stable structural configuration and the corresponding electronic properties based on GGA (Generalized Gradient Approximation) functional. In addition, two mixed halide variants like $Cs_2SnGeI_3Br_3$ and $Cs_2SnGeBr_3Cl_3$ are also simulated. The structures show a broadly tunable bandgap of 0.46 to 1.45 eV by the substitution of various halides in the mixed sn-Ge-based perovskite. The halide perovskites show ambipolar transport behavior with long diffusion lengths. The charge density and electronegativity difference analysis show the predominant ionic nature between the Cesium and halogen atoms and the covalent nature of bonding between the Tin/Germanium and halogen atoms. In the mixed halides, an asymmetric charge distribution is visualized for the first time, which is resulting due to the disproportionate bond strength caused by the difference in the electronegativities of I-Br and Br-Cl. This helps in the manifestation of stereochemically-active lone-pair electrons in Sn and Ge which lead to large variations in the Sn(Ge)-halogen bond lengths and enable the high mobility of the charge carriers. The major optical absorption is due to the transition between the hybridized Sn/Ge(s)-X(p) states to Sn/Ge(p) states. The long charge carrier diffusion lengths and significant covalent bonding interactions can enable in improving the efficiency and structural stability of these materials, making them suitable for solar cell applications.

1. Introduction

The tremendous energy needs of the world, demand novel materials for energy generation from solar radiation. The perovskite-based hybrid materials meet the requirement by having earth-abundant constituent elements and simple processing techniques compared to the conventional silicon-based solar cells. The perovskite materials are versatile, which can accommodate a wide range of elements from the periodic table in the ABX_3 framework. The ABX_3 perovskite structure constitutes the inorganic (Cesium; Cs) or organic cations (Methylammonium, Formaminidium) in the *A*-site, metal cation (Lead; Pb, Tin; Sn, Germanium; Ge) in the *B*-site, and halogen anions (Iodine; I, Bromine; Br, Chlorine; Cl) in the *X*-site. The rapid progress of the perovskites for solar cells has resulted in the efficiencies of 22% for tandem cell configurations (Zhao et al., 2018). The advantages of the perovskite solar materials with respect to manufacturing are: (i) low temperature, solution-based processing, and (ii) possibility of inkjet-printed continuous roll-to-roll production on flexible substrates (Huckaba et al., 2019). The bandgap of the perovskite materials can be widely tuned based on strain which turns the indirect bandgap to direct bandgap and shifting of the Dirac cone feature (Zarabinia and Rasuli, 2021). The perovskite-based materials provide added benefits such as low charge carrier effective mass, long carrier lifetime, widely tunable bandgap, and support transport of both electrons and holes. The disadvantages of these materials are (i) the photo and thermal stability issues, (ii) degradation in atmospheric conditions with major effects due to moisture, (iii) disintegration of the constituent elements, and (iv) toxicity of Lead in the Lead-based conventional hybrid perovskites.

A wide range of techniques was attempted to tackle the stability issue, like alloying various constituents, the substitution of inorganic ions instead of organic molecular cation, polymer encapsulation, and cross-linking approaches. The addition of cross-linkers with 2D/3D

* Corresponding author.
E-mail address: vidyar@annauniv.edu (R. Vidya).

https://doi.org/10.1016/j.solener.2022.09.024
Received 7 March 2022; Received in revised form 28 July 2022; Accepted 13 September 2022
Available online 23 September 2022

engineering has increased the lifespan of the perovskite solar cells by up to one year (Grancini et al., 2017). The stability was also improved by the usage of stable single hole transport layer such as Cu_2ZnSnS_4 (Moghadamgohari et al., 2022) and double hole transport layers which protect the perovskite from being permeated by moisture and oxygen (Zhou et al., 2021; Tien et al., 2021). The toxicity of the lead is avoided by replacing it with tin and germanium metal cation (Gidlow, 2004). The partial substitution of the *Ge* cation in *Sn* sites resulting in mixed Cs_2SnGeX_6 has been experimentally shown to have improved stability by passivating the surface with atmospheric oxygen (Chen et al., 2019).

The effect of halide ions on the structural stability and electronic structure needs attention to mitigate the issues related to the long-term stability of these materials in solar cells. Hence, we have studied the effects of various halide ions in mixed perovskites, which results in the double perovskite structure. The effect of the substitution of halides combined with the mixed metal substitution is studied. The optimized crystal structures by various substitutions of the halides $X = $ I, Br, and Cl in the Cs_2SnGeX_6 compositions were found for tuning the bandgap and for improving the material stability. The influences on the crystal and electronic structures due to the mixed halides were studied by taking the equal stoichiometric substitution of the halides such as $Cs_2SnGe(I_3Br_3)$ and $Cs_2SnGe(Br_3Cl_3)$ in the perovskite structure. We have found the manifestation of lone pairs in the metal cations due to the disproportionate bond strengths, a unique phenomenon observed in the mixed halides which have large implications on the mobility of charge carriers for opto-electronic applications (Hieulle et al., 2019; Knight et al., 2021; Karlsson et al., 2021).

2. Methodology

2.1. Structural optimization calculation

In order to find the ground-state structure, optimization of the parameter of the perovskite structures Cs_2SnGeI_6, $Cs_2SnGeBr_6$, $Cs_2SnGeCl_6$, $Cs_2SnGeI_3Br_3$ and $Cs_2SnGeBr_3Cl_3$ were done using the ABINIT software (Gonze et al., 2009) by minimizing the stress and energy. The BFGS (Broyden–Fletcher–Goldfarb–Shanno) algorithm is used for optimizing the positions of the ions using the gradient of the total energy of crystal structure and Hellman-Feynman forces (Feynman, 1939) acting between the ions. The BFGS is Quasi-Newton minimization of energy for predicting the next step of multiple ion positions in the crystal lattice and is provided with a minimal computational complexity of O (n^2) by incorporating the gradient with curvature information. The Quasi-Newton approach provides minimization without the Jacobian which is computationally expensive and conventionally used in the Full-Newton approach. The stress and forces in the unit cell are minimized and the corresponding ionic positions are found in an iterative manner, where the ion positions are displaced infinitesimally and the total energy is found for each step. The minimum convergence criteria for energy between two successive iterations is set at 10 e^{-5} eV/unit cell and the forces between ions are minimized to 2.5 e^{-3} eV/Angstrom. The VESTA crystal visualization software (Momma and Izumi, 2011) is used for the preprocessing and post-processing of the studied crystal structures.

2.2. Inputs for computation

The electronic calculations were performed using the optimized norm-conserving Vanderbilt Pseudopotentials (ONCVP) (Hamann, 2013) in the ABINIT code employing plane-wave basis set. The pseudopotential portrays the atom by eliminating all-electron states such as the core states of the atom and describes the valence electrons as rapidly decaying wave function in Fourier space. This ONCVP pseudopotential gives good computational efficiency and accuracy. The electron non-locality is implemented using the Legendre polynomial. The Legendre polynomial describes the spherical harmonic distribution of electron wave function around the atom.

The exchange–correlation effects of the electrons are solved using the GGA-PBE (Generalized Gradient Approximation Perdew-Burke-Ernzerhof) (Perdew et al., 1996). The GGA predicts the inhomogeneous electron distribution in the crystal structure by taking into account both the density and gradient of the density, which incorporates the locality and non-locality of the electrons. The PBE functional is parameter-free and applies to a wide range of systems. The electron density predicted by the GGA is used for the analysis of electronic properties like electronic band structure, density of states, bonding behavior, spin-polarization, etc. The lower-lying electrons below the valence electron orbitals are treated as fixed core electrons.

The basis set considered for treating the valence electron orbitals are for Cs – *6s*, Sn – *4d, 5s, 5p*, I – *5s, 5p*, Br – *4s, 4p*, Cl – *3s* and *3p*. The spherical harmonics up to $l = 6$ were used to define the potentials and charge density. The converged parameters used for Cs_2SnGeI_6 structure is the energy cut-off with 1088 eV and a grid of $8 \times 16 \times 8$ k-points. The kinetic energy cutoff allows the number of plane waves in a specific k-point. The total energy reduces as the energy cutoff is increased and leads to the convergence of the ground-state system. The benchmark converged energy cutoff value is used for analyzing other structures.

For the optical calculations, during the self-consistent field calculation, the tolerance of the potential difference for self-consistent field iteration to stop is set to 2.7 e^{-8} eV, and tolerance of wavefunction squared residual is 7.4 e^{-20} eV^2. The broadening of 0.05 eV is applied to the optical plots. For the susceptibility calculation in the optical plots, the fineness of the grid to calculate the energy eigen value ($\delta\omega$) is taken as 0.008 eV and maximum photon energy is given as 8.16 eV.

3. Results and discussion

3.1. Geometric structure

The studied ABX_3 perovskite structural parameters and crystal structure are shown in Table 1 and Fig. 1, respectively. The *A*-site cations originally occupy the corner positions and *B*-site atoms in the body-center positions in the regular perovskite structure. In the present system, as two *B*-site cations (Sn, Ge) occupy the body-center positions, the unit cell is doubled, making the *A*-site atoms occupy the corner as well as edge-center positions, with 12 coordinations, resulting in the double perovskite structure. The two *B*-site cations (Sn, Ge) present inside the unit cell, have 6-fold coordinations with the surrounding *X*-site (I, Br, Cl) halogen anions, which form the metal-halide BX_6 octahedral network. The pristine halide and mixed halide structures are tetragonal, with the space group *P4/mmm* and *P4mm* symmetry, respectively. As the GGA takes into account the gradient of the charge density, it underestimates the binding between the atoms. So, GGA overestimates the length of lattice parameters. The unit cell of the crystal structures with the estimated lattice constants are shown in Table 1. The crystal structure is ordered with the distribution of the Sn, Ge metal cations distributed alternatively along the *b*-axis.

The loosely hinged BX_6 octahedra formed by the sn-*X*, and Ge-*X* bonds, result in the dynamic structural changes of the crystal structure. This leads to the different phases of the perovskite crystal structures, by the mechanism of octahedral tilting and distortions (Stoumpos and Kanatzidis, 2015). There is no octahedral tilting in the studied pristine and mixed halide structures. The reduction in the symmetry from *P4/mmm* for the pristine structure to *P4mm* for the mixed halide structure is due to the substitution of mixed halides and the second-order Jahn-Teller distortion in comparison with the *Pm* 3 *m* cubic symmetry (Stoumpos and Kanatzidis, 2015).

Compared to the organic molecular cation (at the *A*-site), the Cs ion is heavy and its single atomic charge density is spherically distributed. So, the dynamic vibration effect of Cs is less compared to the organic molecular cation. The Cs ion also influences the phase transition and has high phase transition energy which results in higher thermal stability of the structure compared to the structures with the organic molecular

Table 1
Structural Parameters and band gap of the crystal structures show decreasing trend in lattice parameters and increasing trend of bandgap with the substitution of smaller and more electronegative halides. Bold value shows the computed lattice parameter taken from the literature.

Compound	Volume ($Å^3$)	Atomic packing factor (%)	Lattice Parameters (Å)			Calc Band gap (eV)	Expt Band Gap (eV)
			a = c	b	α = β = γ	SR-DFT	
Cs_2SnGeI_6	464.56	77.8	6.155	12.262 (**11.50**[#])	90	0.91	(1.50[*])
$Cs_2SnGeI_3Br_3$	434.2	78.7	6.012	12.013	90	0.46	–
$Cs_2SnGeBr_6$	381.78	83.4	5.767	11.478	90	1.15	–
$Cs_2SnGeBr_3Cl_3$	364.82	84	5.668	11.353	90	0.82	–
$Cs_2SnGeCl_6$	331.72	87.4	5.504	10.951	90	1.45	–

[*] Ref: (Chen et al., 2019).
[#] Ref: (Liu et al., 2021).

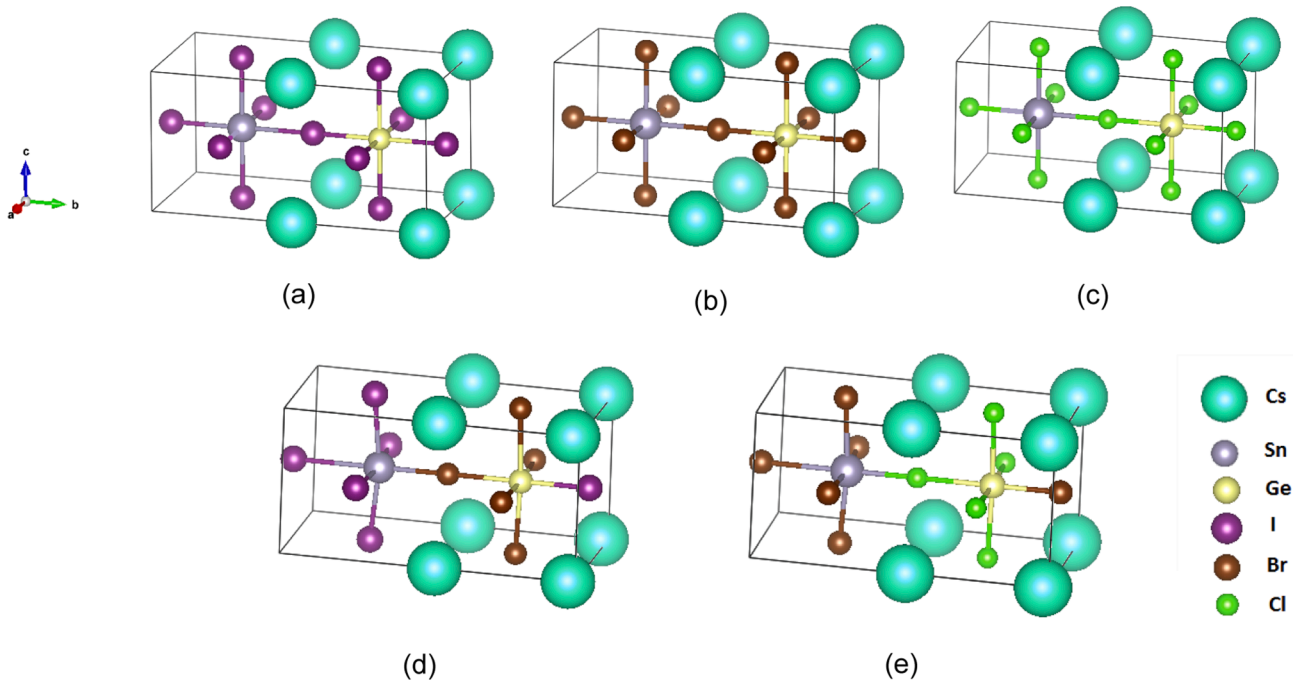

Fig. 1. Unit cell of the (a)Cs_2SnGeI_6, (b)$Cs_2SnGeBr_6$, (c)$Cs_2SnGeCl_6$, (d)$Cs_2SnGeI_3Br_3$ and (e)$Cs_2SnGeBr_3Cl_3$ structures.

cations (Hu et al., 2018). The structure undergoes a phase transformation from low-temperature triclinic to high-temperature cubic phase. The order of transformation is from triclinic to monoclinic - orthogonal - tetragonal - cubic structure (Feng and Xiao, 2014).

The total volume corresponding to the lattice parameter plot shows that the volume and lattice parameters are reduced due to the substitution of I with Br, Cl. The lattice parameter of the Cs_2SnGeI_6 structure is compared with the computationally predicted cubic structure by Liu et al. (Liu et al., 2021). There is a direct effect of the smaller halide anions substitution in the atomic packing factor of the unit cell, which is calculated using the van-der-Waals ionic radii using Platon software (Spek, 2003).

As shown in Table 1, the packing factor reduction is 7% for substitution of I with Br, and 5% for substitution of Br with Cl. The value of the total volume of the intermediate structures of the mixed halides lies between the volumes of the pristine halide structures. The chlorine substituted structure shows the highest packing factor compared to other structures. The variation between the unit cell volumes and packing factor directly correlates with the increase in experimental ionic radii of the substituted halides I, Br, and Cl, which are 2.20, 1.96, and 1.85 Å, respectively.

For pristine halide structures, the bond length variation between various metal cations with the halide anions for the alloyed structure is shown in Table 2. The comparison of the sn-*X* bond with the Ge-*X* bond, in the Cs_2SnGeX_6 structure, shows that the sn-*X* bond is longer than the Ge-*X* bond. This is attributed to both the ionic radii and the electronegativity of the metal cation. The Ge has lesser effective (Shannon)

Table 2
Bond length, angles and bond ratios of the perovskite structures shown for various halide substitutions.

Compound	Sn-X bond length (Å)		Ge-X bond length (Å)		Bond ratio	Sn-Br-Sn bond angle (deg)	
	min, max	Δ	min, max	Δ	Sn-X/ Ge-X	X-sn-X	X-Ge-X
Cs_2SnGeI_6	3.077, 3.156	0.079	2.974, 3.077	0.103	1.06	180	180
$Cs_2SnGeI_3Br_3$	2.791, 3.479	0.688	2.790, 3.008	0.218	1.25	169	175
$Cs_2SnGeBr_6$	2.883, 2.968	0.085	2.770, 2.883	0.113	1.07	180	180
$Cs_2SnGeBr_3Cl_3$	2.655, 3.260	0.605	2.583, 2.854	0.271	1.26	173	177
$Cs_2SnGeCl_6$	2.630, 2.751	0.121	2.751, 2.844	0.093	1.08	180	180

ionic radii of 0.73 Å compared to that of Sn with 1.15 Å. The electronegativity (as per the Pauling scale) of Ge (2.01) is slightly more than that of Sn (1.96). The ionic radii play an important role in deciding the bond length because the difference in the electronegativity of halides is small. The ratio of the sn-*X* to *Ge-X* bond length made with the commonly shared halide cation (*X*) is 1.06, 1.07, and 1.08 for I, Br, and Cl, respectively. Table 2 shows the increase in the bond ratio which is due to the substitution of the smaller ionic radii and more electronegative anion [I (2.66) < Br (2.96) < Cl (3.16)]. For the pristine halide structures, the bond length variation of the metal octahedral coordination with the halides shows a wide variation in the Ge-*X* bond length compared to the sn-*X* bond length, except for the Cl structure. The bond angles of the Sn and Ge with the surrounding halides in the axial and equatorial directions form 180° with an undistorted octahedral structure.

The mixed halides show a reverse trend in the variation of the sn-*X* bond lengths resulting in the long-short alternation with the halide compared to the Ge-*X* bond lengths. This is due to the non-symmetrical coordination of the Sn and Ge ions with the mixed halides as shown in Fig. 1(d) and (e). For the mixed halide structures, this bond length variation is mainly because, the more electronegative halides prefer closer proximity to Ge, whereas the less electronegative halides prefer proximity to the Sn ion. The mixed halide structures show octahedral distortion, which results in the deviation of the bond angle from the pristine halide structures, exhibiting 180° with intact octahedral structure (see Table 2).

The tolerance factor (TF) is the dimensionless ratio of ionic radii of the atomic constituents present in the perovskite structure. The formula to calculate the TF is given in the Eq. (1). The empirical optimal stable range of tolerance factor for perovskite structure formation is 1.1 > T.F > 0.9 (Becker et al., 2017). When the TF crosses the optimal range, there is significant distortion in the octahedra and the perovskite structure stabilizes in the structures with lower symmetries.

$$TF = \frac{r_A + r_X}{\sqrt{2(r_B + r_X)}} \tag{1}$$

The octahedral factor (OF) validates the proper octahedral coordination of the metal cations with the surrounding six halide anions, which is calculated using Eq. (2). When the octahedral factor is less than 0.414, the octahedra becomes unstable due to the low coordination number. On the other hand, when octahedral factor is >0.592, it results in the accommodation of 7 anions in contact with the metal cation.

$$OF = \frac{r_B}{r_X} \tag{2}$$

The TF for all three structures is close to the value of 0.9, which implies the structural stability of the sn-Ge-based perovskites (see Table 3). The tolerance factor is calculated by replacing the ionic radii (r_B) of the metal with the average ionic radii of Sn and Ge, because of the equal number and contribution of the Sn and Ge present in the unit cell. The octahedral factor shows the suitable size of the metal cation for the corresponding halides. The octahedral factor of the Sn cation (0.44–0.62) shows a stable value (Octahedral Factor > 0.44) for all three different halides. The octahedral factor of the Germanium (0.35–0.39) is below the stability range. However, the averaging of the octahedral factors of mixed sn-Ge perovskite relatively stabilizes the structure compared to the pristine Germanium-based perovskite. For the mixed halides, the I-Br shows the highest TF compared to other structures, which predicts the mixed halide structure to be relatively stable compared to the single halide structure. The average octahedral factor for the mixed halides I-Br and Br-Cl is within the range of the single halide parent structures with I, Br, Cl.

Table 3
Tolerance Factor and Octahedral Factor of the crystal structures.

Compound	TF	OF		
		Sn-X	Ge-X	Avg
Cs_2SnGeI_6	0.892	0.441	0.35	0.396
$Cs_2SnGeI_3Br_3$	0.905	0.441	0.372	0.407
$Cs_2SnGeBr_6$	0.889	0.587	0.372	0.480
$Cs_2SnGeBr_3Cl_3$	0.889	0.587	0.395	0.491
$Cs_2SnGeCl_6$	0.897	0.622	0.395	0.509

3.2. Electronic properties

Sn-Ge perovskite structures have Valence Band Maximum (VBM) and Conduction Band Minimum (CBM) at the same momentum vector point (*A* k-point), resulting in the direct bandgap. The direct bandgap enables the transition of electrons from VBM to CBM, only with the absorption of photons and it is not assisted by the phonons due to the crystal momentum. The calculated bandgap using GGA is 0.91, 1.15, 1.45 eV for Cs_2SnGeI_6, $Cs_2SnGeBr_6$, $Cs_2SnGeCl_6$ structures, respectively. The experimental bandgap of the mixed metal cation Cs_2SnGeI_6 (1.5 eV) based perovskite lies between the experimentally reported bandgap of the pristine structures, $CsSnI_3$ (1.63 eV) and $CsGeI_3$ (1.34 eV) (Chen et al., 2019). The GGA functional underestimates the bandgap by 0.59 eV, due to the over binding of the lattice parameter which is inversely proportional to the calculated bandgap. The conduction bands of the Br, Cl substituted structures experience a blue shift compared to the Iodine structure, due to the increase in the electronegativity of the substituted halides, resulting in the increasing trend in the bandgap for Cl, Br, and I halide cations. The VBM and CBM of all the studied systems are well-dispersed indicating higher hole and electron mobilities.

The electronic structure of the Cs_2SnGeI_6 has 45 bands within the energy range of −8 to 8 eV. The bands denote the range of energy level continuum that the electron can occupy in the crystal. The bands occupying the corresponding position in energy scale are grouped into valence band and conduction band regions, (i) from −8 to −6 eV region has 2 bands with peaks of *Ge 3s* at −8eV, (ii) from −6 to −4 eV is devoid of any band, (iii) from −4 to 0 eV region has 18 bands with peaks of *Sn 5s* at −0.73 eV, *Sn 5p* at −3.92 eV, *Ge 4s* at −1.34 eV, *Ge 4p* at −3.76 eV and *I 5p* at −1.83 eV, (iv) from 0 to 4 eV region has 4 bands with peaks of *Sn 5p* at 1.73 eV, *Ge 4p* at 1.47 eV. (v) from 4 to 8 eV region has 21 bands with *Sn 5p* and widely dispersed contribution from Cesium. A prominent well-dispersed band seen at the VBM is contributed by the hybridization of *sn-s* and *I-p* orbitals, and that at CBM is due to *Sn* and *Ge-p* orbitals. Hence, the mobility of electron and hole charge carriers will be high.

The $Cs_2SnGeBr_6$ structure has a total number of 45 bands. The grouping of bands within the energy range, (i) from −7 to −6 eV region has 2 bands, (ii) from −6 to −4 eV region has 5 bands, (iii) from −4 to 0 eV region has 13 bands with peaks of *Br 4p* shifted away from the Fermi level compared to *I 4p*, (iv) from 0 to 4 eV region has multiple peaks of *Sn 5p* and *Ge 4p*, (v) from 4 to 8 eV region has 22 bands with peaks of *Sn 5p* and widely dispersed contribution from *Cs* ion. Compared to the Cs_2SnGeI_6, the presently considered $Cs_2SnGeBr_6$ has more dispersed VBM, whose major contribution arise from the hybridization of *Sn* and *Br-p* states. A relatively dispersed band is seen along the R-A-Z direction resulting due to the hybridized *Ge* and *Br-p* states.

The $Cs_2SnGeCl_6$ structure has 47 bands. The valence and conduction bands contributions are grouped as, (i) from −8 to −6 eV region has 7 bands, (ii) from −6 to −4 eV region has 5 bands, (iii) from −4 to 0 eV region has 13 bands with peaks of *Cl 3p*, (iv) from 0 to 4 eV region has 3 bands, (v) from 4 to 8 eV region has 19 bands with widespread contribution from Cesium atom similar to the other two structures. The valence band and conduction band peaks are dispersed and move away from the Fermi level for the Br and Cl in comparison with the Iodine structure. Among the three pure halide compounds, $Cs_2SnGeCl_6$ has the most well-dispersed VBM resulting due to the *sn-s* and *Cl-p* states. The well dispersed band seen close to the VBM along the R-A-Z direction originated from the hybridization of *Ge-s* and *Cl-p* states. In all the three compounds Cs has mainly ionic bonding, whereas Sn and Ge-*X* bonding

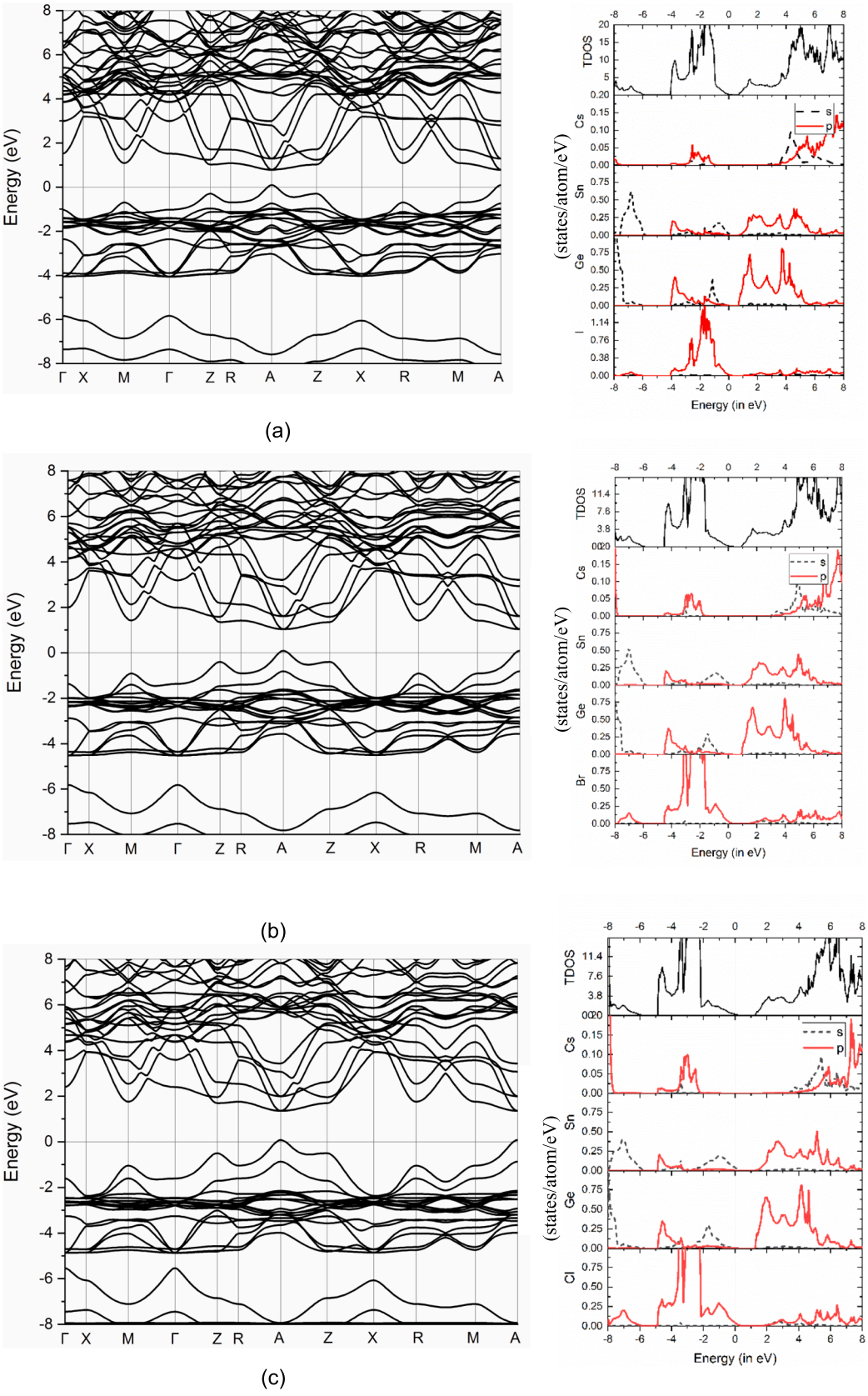

Fig. 2. Band structure and partial density of states of the (a)Cs_2SnGeI_6, (b)$Cs_2SnGeBr_6$, (c)$Cs_2SnGeCl_6$, (d)$Cs_2SnGeI_3Br_3$ and (e)$Cs_2SnGeBr_3Cl_3$ structures, which shows major contribution from Sn, Ge in the Valence band and Halide contribution in the Conduction band.

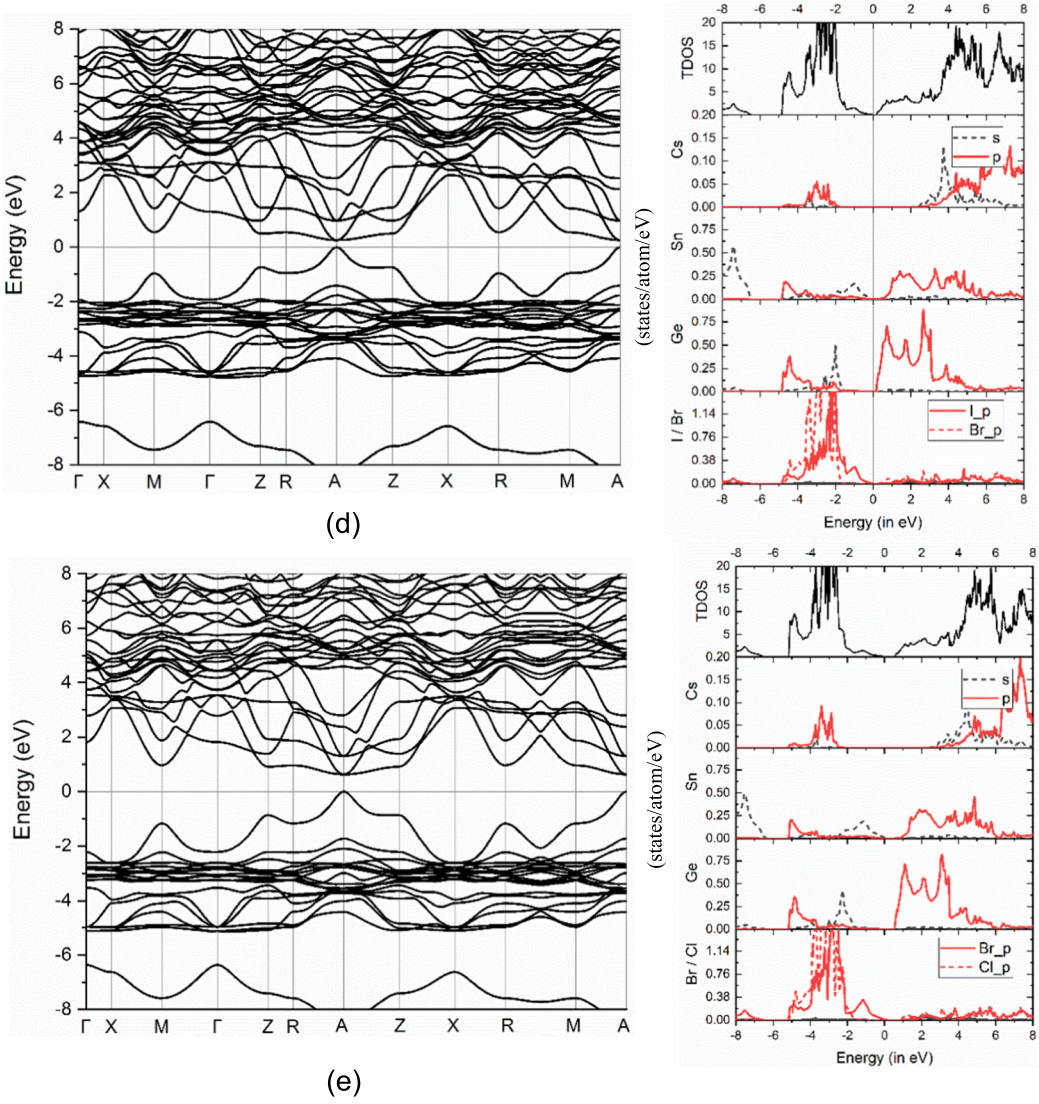

Fig. 2. (*continued*).

has mixed bonding nature with predominant covalent character.

The mixed halide structures such as $Cs_2SnGe(I_3Br_3)$ and $Cs_2SnGe(Br_3Cl_3)$ have a total of 45 and 44 bands, respectively. Interestingly, when the *X*-site is occupied by I/Br or Br/Cl, the bandgap value reduces mainly due to the p-orbitals of Sn and Ge present at the CBM are lowered in energy. More importantly, a clear isolated band can be seen at VBM (Fig. 3d, e), which is delocalized and spans an energy range of >2.2 eV. This implies that the hole conductivity will be higher due to its small effective mass. This well dispersed band is contributed by hybridization of sn-*s* and *X-p* orbitals. The lone-pair electrons at Sn evinced due to the presence of mixed halogen atoms also contribute to the increased width of this band. Moreover, the direct bandgap nature is preserved even if the mixed halogens are present. Therefore, optical absorption can be enhanced because Fermi's Golden rule for optical transition is satisfied.

The partial density of states (PDOS) (Fig. 3a-e) plots of all the three structures show that the VBM consists of a major contribution from *I 5p*, *Br 4p*, *Cl 3p*, and a minor contribution from *Sn 5s, Ge 4s* orbitals. The CBM shows the major contribution from the *Sn −5p* and *Ge-4p* states. The substitution of the Iodine with Bromine and Chlorine, which have smaller ionic radii [I (2.20 Å) >, Br (1.96 Å) > Cl (1.85 Å)], results in the lattice contraction and the B-*X* bond length reduction. The substitution of the smaller and more electronegative anion [I (2.66) < Br (2.96) < Cl (3.16)], results in the blue shift of the lowest-lying conduction bands directly affecting the bandgap of the material. The PDOS results show the shift of halides valence level *p*-orbitals peaks away from the Fermi level [I (*5p*) < Br (*4p*) < Cl (*3p*)], which also influences the peak photon absorption energy level. In all the three pure halides, the Cs atom contains negligible DOS (Density of states) as it has donated most of its electrons to the halogen atoms, forming ionic bonding between Cs-*X*. The DOS in the −5 to 0 eV range is mainly contributed by *s* and *p-orbitals* of Sn, Ge and *p-orbitals* of *X*. As these orbitals are energetically and spatially degenerate, they form significant covalent bonds. In fact, the BX_6 octahedra (eg $SnCl_6$ and $GeCl_6$) formed as a combined unit by the above mentioned bonding interaction, forms ionic bonding with Cs atom $[Cs_2^{2+}(SnGeI_6)^{2-}]$.

The size of the Cesium ion acts as the structural spacer and charge neutralization of the crystal lattice charge fields. This in turn holds the sn-I_6 octahedra, reducing the tilt and rotation due to the highly stabilized renormalization of vibrations provided by the Cesium ion. This is symmetrical compared to the non-symmetrical molecular cation such as Methylammonium and Formaminidium (Patrick et al., 2015; Raja et al., 2020).

The PDOS of mixed halides (shown in Fig. 2), for the I-Br and Br-Cl structures exhibits similar individual atomic electron density contributions of halides compared to the pristine single halide structures. There is a significant redshift of the Tin and Germanium bands, compared to

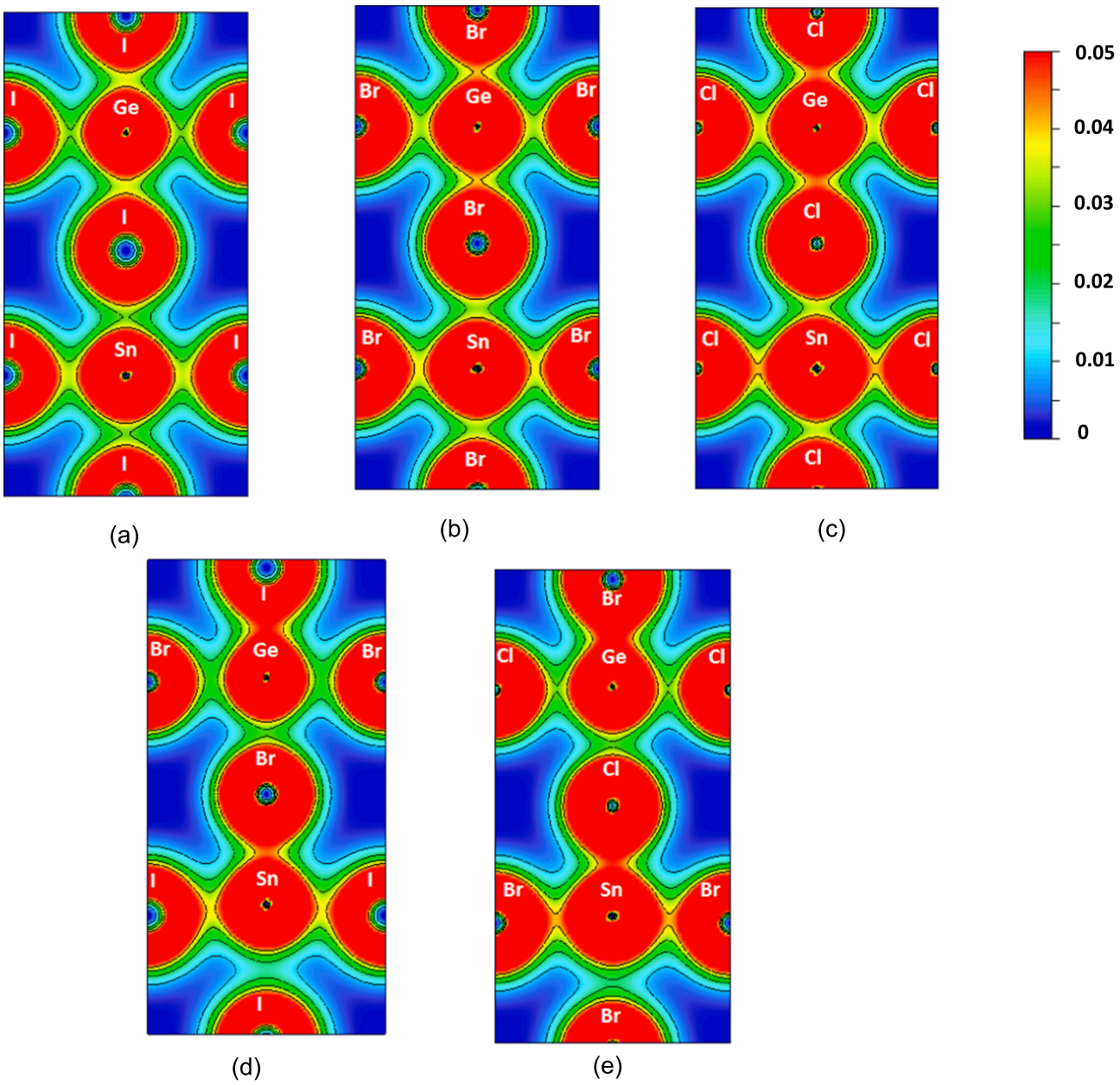

Fig. 3. Charge density plots of the (a)Cs_2SnGeI_6, (b)$Cs_2SnGeBr_6$, (c)$Cs_2SnGeCl_6$, (d)$Cs_2SnGeI_3Br_3$ and (e)$Cs_2SnGeBr_3Cl_3$ structures, which show the electron density shared between the metal cations and halide anions show polar covalent bonding.

the constituent pristine halide structures, which results in the reduction of the bandgap. This is due to the non-symmetrical coordination of metal ions with the mixed halides, the wide variation in their BX_6 bond lengths, and more electronegative and smaller anions being placed in closer proximity to the Ge anion in the low energy structure, leading to the redshift of the bands contributed by the metal ions. The substituted halide structures result in the broadly tunable bandgap with the closely fitting lattice parameters which can be applied to form functionally graded materials for solar energy applications.

In addition, the PDOS of the individual atoms undergo noticeable changes together with halide ions. Even though Cs-X bonds remain ionic, the sn-*s* and Ge *s* and *p* orbitals are changed; *sn-s* states becomes more delocalized leading to highly dispersed band at the top of the valence band, which enhances the mobility of the charge carriers. On the other hand, the *s* and *p*-states of Ge becomes more localized with sharp peaks. The I/Br and Br/Cl *p*-states form strong hybridization with the *Ge-s* levels, close to −2eV energy range, making the next higher valence band also to be wide. Interestingly the number of states of halide ions increases as evidenced by the significant increase in the height of the respective peaks.

The electronic charge density plots which provide the atomic-level details on the bonding characteristic of Cs_2SnGeX_6 (X = I, Br, Cl) are shown in Fig. 3a-3c. The electronegativity differences between Sn and I/Br/Cl are 0.62, 0.9 and 1.12 respectively, and that between Ge and I/Br/Cl are 0.56, 0.80, and 1.06, respectively. As the range of electronegativity difference is between 0.4 and 2.0, these bonds have polar covalent nature, in addition to being ionic.

A closer look at the charge density plot together with PDOS reveals that the bond between Ge-Cl is stronger than the other Ge-*X* counterparts. More DOS seen between Ge and Cl in the −2 to 0 eV range and denser charge density seen in Fig. 3c, seem to support this view point. However, the electron localization function (ELF) given in Fig. 4a-4e, which provide information on paired-electron distribution paints a different picture. It may be noted that high ELF value (>0.5 to 1) implies

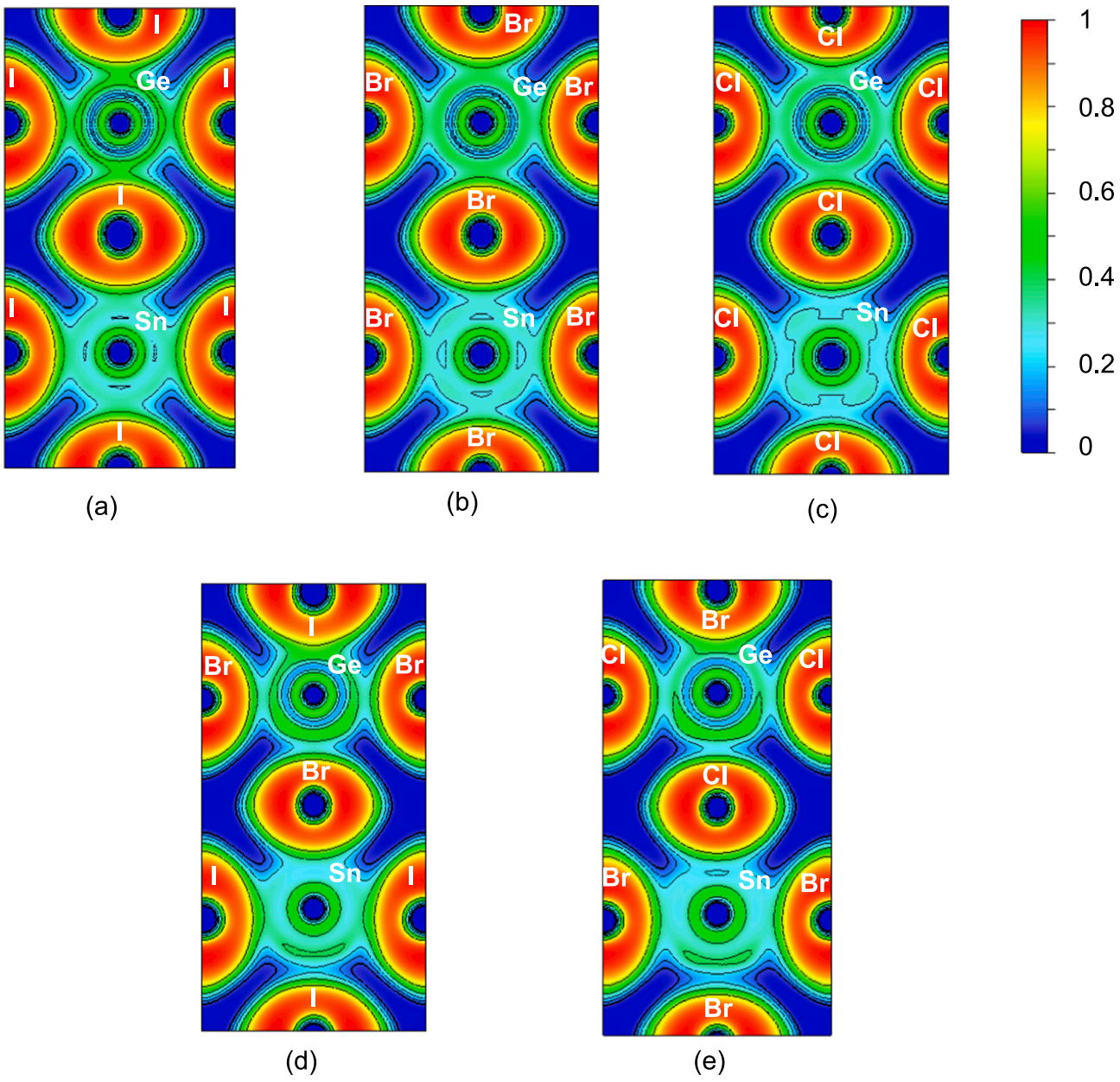

Fig. 4. Electron Localization Function plots of (a) Cs_2SnGeI_6, (b) $Cs_2SnGeBr_6$, (c) $Cs_2SnGeCl_6$, (d) $Cs_2SnGeI_3Br_3$ and (e) $Cs_2SnGeBr_3Cl_3$ structures, which shows the bonding nature between the atoms.

more covalent character. As Ge-I bonds have more ELF contours than Ge-Cl, it can be concluded that the covalent interaction of Ge-I is more than that of Ge-Cl. This may be because, the Cs cation retains more *s*-electrons in the $Cs_2SnGeCl_6$ compound compared to the other two halogen variants. As Cl is the most electronegative element compared to I and Br, it attracts more electrons from Cs, than the other halogens making its ionic bonding character significant.

The charge density plots show that the bonds of the metal halide are predominantly polar covalent, and become more ionic as we replace I with Br and Cl, due to the increase in electronegativity of the halogen anion which strongly pulls the electrons from the metal cation towards itself. The same results in the more dispersed charge density due to the screening effects of core-level electrons of the Iodine (*5p*) and gets more concentrated for the Br(*4p*) and Cl(*3p*) substituted structures.

The charge density between the Cesium and the neighboring halide anions is localized for each ion and separated, showing predominantly ionic bond formation between the Cesium ions with the halide anions. The electronegativity difference between the Cs and I/Br/Cl bonds is 1.87, 2.17, and 2.37, respectively. The range is closer and above 2, so the bonds are strongly ionic. The inorganic cation Cesium plays an important role in the charge carrier, reduction of trap states, and stability of the material (Hu et al., 2018).

In the case of mixed halide structures, the sn-*X* and Ge-*X* bond distances are highly varying (as given in Table 2). Among the all five studied compounds, the bond length variation in $Cs_2SnGeI_3Br_3$ is the maximum. This may be due to the fact that the ionic radii of Br and Cl differ by 0.15 Å, whereas that between Br and I differ by 0.24 Å. The bond length between sn-*X* and Ge-*X* is the least in the case of $Cs_2SnGeBr_3Cl_3$ among all the five compounds.

Upon comparing the charge density around Sn and Ge atoms in the pristine (Fig. 3a–c) with that of the mixed halides (Fig. 3d and e), significant difference in their distribution can be observed. Therefore we have plotted the ELF for these systems in the same crystallographic planes. The electron localization around Sn and Ge in the pristine

compounds are uniform (Fig. 4a-c), whereas more ELF is seen along the *b*-axis around Sn and Ge in the case of $Cs_2SnGeI_3Br_3$ (Fig. 4d) and the asymmetry in the ELF is further enhanced for $Cs_2SnGeBr_3Cl_3$ (Fig. 4e). The asymmetric charge distribution and ELF in the mixed halides is a clear signature of the lone-pair electrons in Sn and Ge (Ravindran et al., 2006; Fabini et al., 2020; Smiles et al., 2021). It can be inferred that in the mixed halides, the variation in the ionic radii and electronegativity of I/Br and Br/Cl causes disproportionate bonding interactions between Sn/Ge and the halogen atoms, resulting in the manifestation of lone-pair electrons of Sn and Ge. These lone-pair electrons are in fact stereochemically active as evinced by the enhanced binding hybridization interactions between sn-*s* and *X-p* orbitals, resulting in a very broad band at VBM which has dispersion of ~ 2.5 eV. Hence, the holes can be light and their mobility will be high for these mixed halide compounds.

The effective mass of the charge carriers is calculated by approximated curve fitting of the parabolic equation of momentum *k* to the bands as shown in the Eqs. (3) and (4) below.

$$E = \frac{\hbar^2}{2m}k^2 \tag{3}$$

$$m = \hbar^2\left\{\frac{\partial^2 E}{\partial k^2}\right\}^{-1} \tag{4}$$

The effective mass of the charge carriers of the pristine and mixed halide structures is shown in Table 4, with an overall increase in the effective mass of the electrons as we substitute Iodine with the more electronegative Br, Cl anions. The halide with more electronegativity creates a stronger pull of electron towards itself, resulting in higher binding energy which, in turn widens the bandgap. The lower dispersion or curvature of the conduction bands results in the increased effective mass of electrons.

In order to obtain a quantitative idea about the mobility of charge carriers in the studied systems, we have calculated the hole and electron effective mass close to the VB and CB edges (Viz,. R-A, A-Z and X-R) directions of the first Brillouin zone. In the band structure plots shown in the left panels of Fig. 2a-e, it is clear that an isolated broad band occurs close to the VBM whereas two strongly-hybridized degenerate bands occur at the CBM. These hybridized bands seen at the high symmetry A-point in the CBM is the result of Sn and Ge *p* states. We have calculated the effective mass of hole and electron by applying the Eqs. (3) and (4) on these disperse bands.

It can be inferred from Table 4 that all the studied compounds have almost similar hole and electron effective masses. The low values of these effective masses imply that the mobility of charge carriers is significantly high. Even though the mixed halides show highly dispersed band at the top of VB, their effective masses are similar to that of pristine compounds along the considered R-A, A-Z and X-R direction. As the mobility is inversely correlated with the effective mass, the halide perovskites show ambipolar behavior and large diffusion length for both electrons and holes.

3.3. Optical properties

The optical response of the Cs_2SnBrX_6 using the GGA approximation for the external electromagnetic perturbation over a wide range of optical frequencies is studied. The optical properties are calculated by the complex dielectric function, ε (ω, q) which models the light-matter interaction. The dielectric function is determined by the frequency (ω) of the photon and the wave vector (q) corresponding to the photon-to-electron momentum transfer. The effect of momentum is negligible compared to the frequency. So, it is not considered in the calculation. The dielectric function has the real and imaginary parts as shown by the following formulae in Eq. (5).

$$\varepsilon(\omega) = \varepsilon_1(\omega) + i.\varepsilon_2(\omega) \tag{5}$$

The dielectric function calculated for the *a, b,* and *c* directions of the unit cell is shown in Fig. 5. The optical anisotropy of the studied compounds along the *b*-axis is due to the alternation of the metal cations forming sn-I-Ge bonds. The same trend is visible for all the structures, where I anion is replaced by Br and Cl. The increase in optical response is in the order of I > (I-Br) > Br > (Br-Cl) > Cl, due to (i) the electronegativity difference of the halides, (ii) bandgap, and (iii) the energy level of the *p*-orbitals of the halide anion in the valence band and (iv) the *p*-orbitals of the metal cation in the conduction bands. The low electronegativity of the Iodine ion allows valence electrons to be excited at lower energies compared to the Br, Cl.

The Iodide pristine structure has a dominant peak at 2.31 eV. For the Bromide and Chloride pristine structures, there are many significant peaks spread across the energy range from 2 to 8 eV. The Bromide pristine structure has three dominant peaks at 2.87, 3.78, and 4.6 eV which are shifted compared to the Iodine structure. The Chlorine-based structure has similar three dominant peaks at 2.45, 2.95, and 3.44 eV with a lower magnitude of optical response than the Bromide structure.

The correlation of the computational result with the experimental results can be made by evaluating the following optical properties such as absorption coefficient, reflectivity, and refractive index. The absorption coefficient shows the frequency-dependent absorption of the electromagnetic radiation in the semiconductor through electron transition from the valence to the conduction band. The reflectivity is derived from the complex index of refraction and shows the reflectivity response of the material for various photon wavelengths. The refractive index shows the measure of the speed of light inside the material, relative to the vacuum and also gives the polarizability property of the material. The Fresnel equations (Eqs. (6), (7) and (8)) are used to calculate the reflectivity (R), absorption coefficient I (ω), and refractive index (n), which are shown in Fig. 5a-f.

$$R(\omega) = \left|\frac{\sqrt{\varepsilon(\omega)} - 1}{\sqrt{\varepsilon(\omega)} + 1}\right|^2 \tag{6}$$

$$I(\omega) = 2\omega\left[\frac{|(\varepsilon(\omega))| - \varepsilon_1(\omega)}{2}\right]^{\frac{1}{2}} \tag{7}$$

$$n = \left[\frac{|(\varepsilon(\omega))| + \varepsilon_1(\omega)}{2}\right]^{\frac{1}{2}} \tag{8}$$

The optical absorption is higher for the Iodine structure compared to the Br, and Cl structures. The peaks in the absorption plot of Cs_2SnGeI_6 structure as shown in Fig. 6b, in the range of 2–3 eV matches with the computational study of Liu et al. (Liu et al., 2021) with maximum value

Table 4
Effective mass of the structures shows general increasing trend of electron and hole mass with the substitution of halides.

	Effective hole mass,m_h^*				Effective electron mass, m_e^*			
Structure	R-A	A-Z	X-R	Avg m_h^*	R-A	A-Z	X-R	Avg m_e^*
Cs_2SnGeI_6	0.39	0.31	0.44	0.38	0.26	0.29	0.28	0.38
$Cs_2SnGeI_3Br_3$	0.33	0.38	0.33	0.35	0.33	0.39	0.36	0.36
$Cs_2SnGeBr_6$	0.34	0.33	0.39	0.35	0.25	0.3	0.29	0.28
$Cs_2SnGeBr_3Cl_3$	0.33	0.39	0.33	0.35	0.33	0.40	0.36	0.36
$Cs_2SnGeCl_6$	0.33	0.38	0.39	0.37	0.28	0.34	0.31	0.31

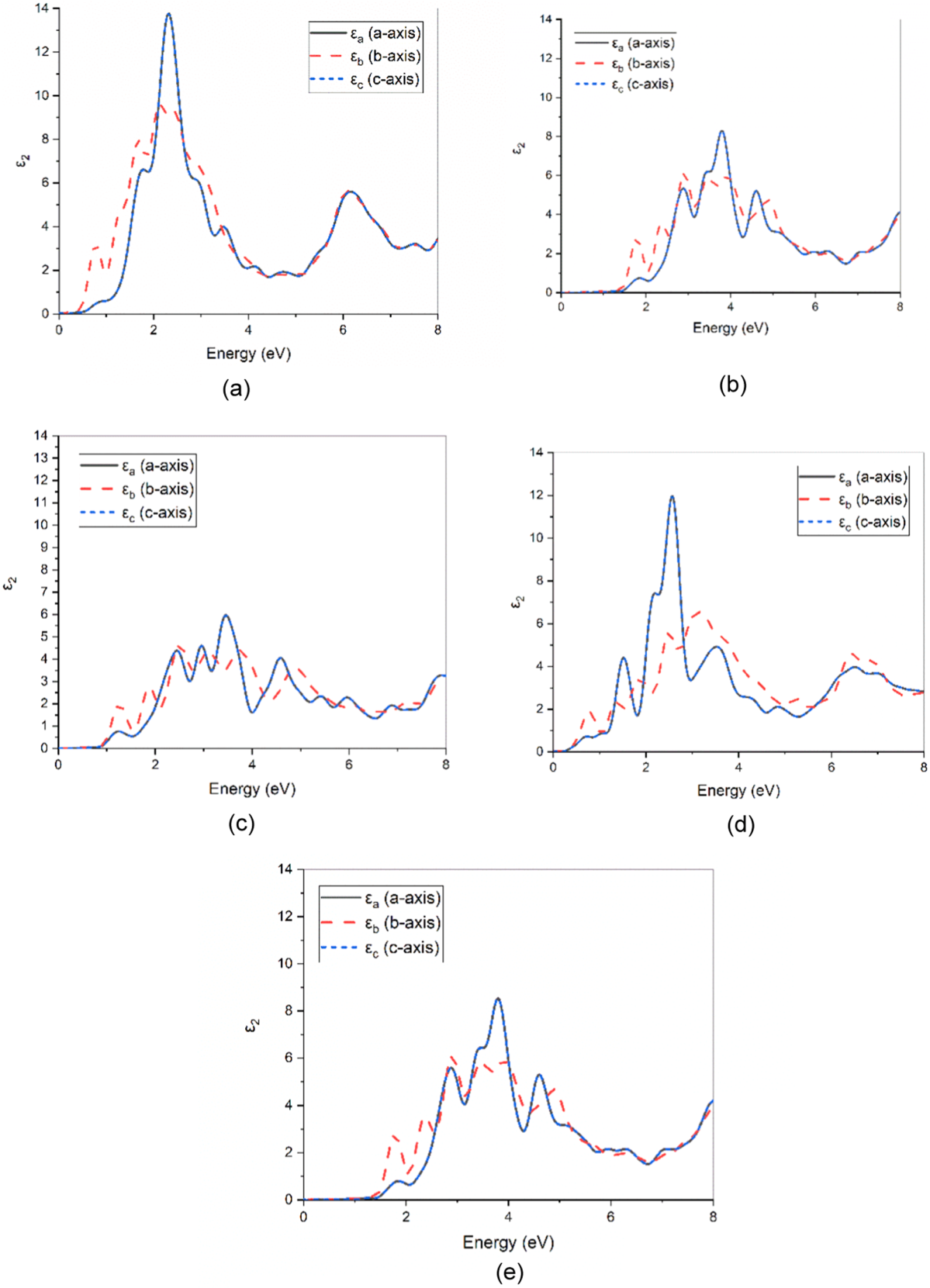

Fig. 5. Dielectric loss function along *a,b,c* directions of the (a)Cs_2SnGeI_6, (b)$Cs_2SnGeBr_6$, (c)$Cs_2SnGeCl_6$, (d)$Cs_2SnGeI_3Br_3$ and (e)$Cs_2SnGeBr_3Cl_3$ structures, which shows better optical response for Iodine structures compared to bromine or chlorine substituted structures.

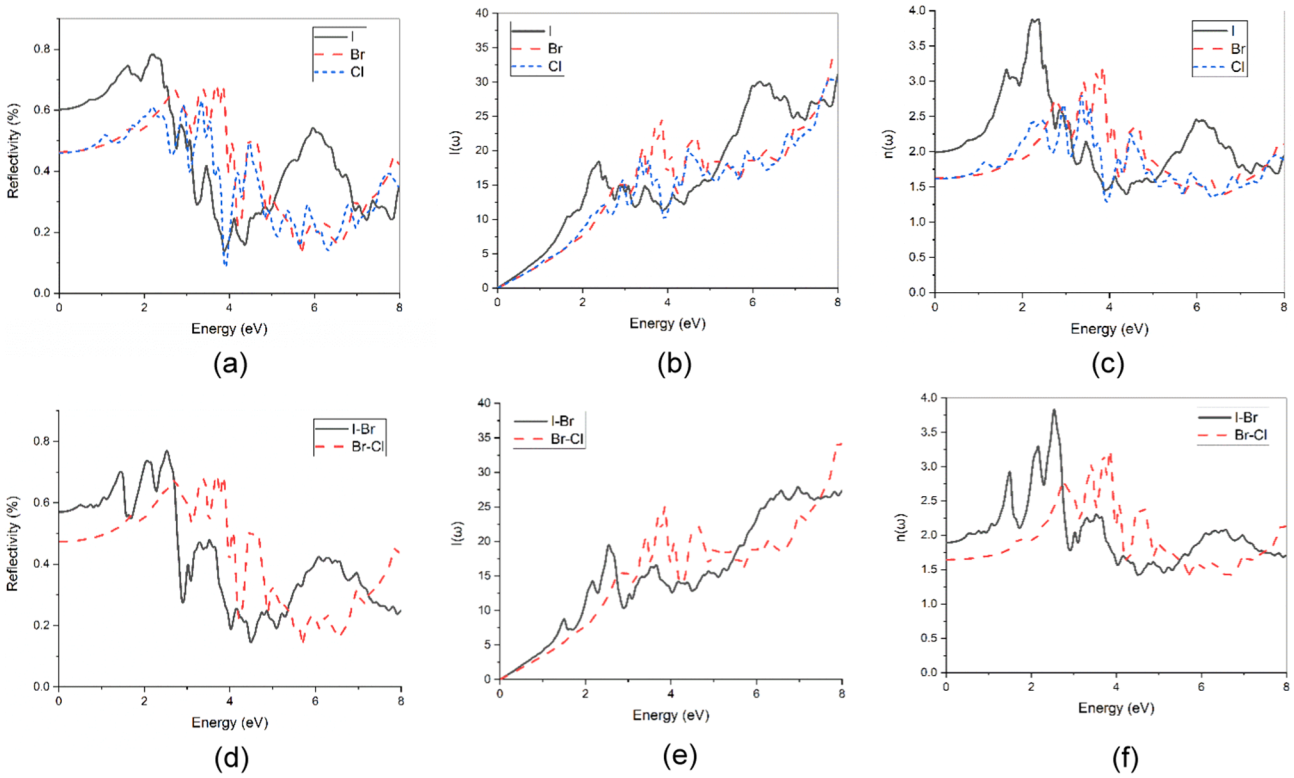

Fig. 6. Reflectivity, absorption, refraction index grouped into pristine structures (a) Reflectivity, (b) Absorption, (c) Refractive index and for mixed-halide structures (d) Reflectivity (e) Absorption and (f) Refractive index.

at 450 nm (2.76 eV) and 550 nm (2.25 eV). The Bromine structure has higher absorption in the narrow region of 3 to 6 eV. The optical reflectivity and refractive index plots show the maximum peak for the 1 to 3 eV range for all three structures. For the mixed halides, the variation in the peak absorption, reflectivity, and refractive index closely correlate with those of the interpolated range of their corresponding single halide structures. The peak in the absorption plot is in the range of 2 to 3 eV for the Cs_2SnGeI_6 structure, which correlates with the external quantum efficiency spectrum reported experimentally (Chen et al., 2019). The dominant peaks for the absorption spectrum are at 2.35, 3.84, and 3.35 eV for I, Br, and Cl pristine structures. For the mixed halides, the dominant peak for the absorption spectrum interpolates that of the pristine structures. The dominant peaks of the absorption spectrum are at 2.54 and 3.85 eV for the mixed I-Br and Br-Cl structures.

The dominant peaks present in the absorption and the dielectric response plots correspond to the transition between the *Sn 5s*, *I 5p* hybridized states in the valence band to *Sn 5p* states in the conduction band. Similarly, dominant peaks correspond to the transition from *Ge 4s, I 5p* hybridized states to the *Ge 4p* states. The Sn and Ge bond with the halide produces allowed electron transition at the high-symmetry A k-point. The substitution of the halide changes band structure properties of the *I 5p* states with corresponding *Br 4p* and *Cl 3p* states.

4. Conclusion

In summary, we have studied the effects of substitution of various halides such as I, Br, and Cl on the properties of mixed-metal and mixed-halogen Cs_2GeSnX_6 in the perovskite structure. The lowest energy lattice for the respective compositions is determined by the structural optimization performed by minimizing total-energy as well as stress and strain. The effects of metal ions such as Sn, Ge, and halogens I, Br, and Cl on the electronic band structure, partial density of states, bonding characteristics, and optical properties are elucidated using various analyses. We have shown that the bandgap of these materials can be effectively tuned by the substitution of various halides. The results show the increasing trend in the bandgap and effective mass as the electronegativity of the halide ion increases and reduction in the corresponding lattice parameters. The band structure and PDOS show that all the structures have a direct bandgap in the range of 0.46 to 1.45 eV. The effective mass of electron and hole shows good ambipolar transport property. The charge density and the electronegativity differences elucidate the predominant covalent nature between the sn-Ge and halide and the ionic nature between the Cs and halide ions. In addition, the electron localization function clearly illustrates the emergence of lone pairs in Sn and Ge in the I/Br, Br/Cl mixed halides. These stereochemically active lone pairs result due to the disproportionate bond strength between Br-sn-I and Br-Sn(Ge)-Cl bonds in the $Cs_2SnGeI_3Br_3$, $Cs_2SnGeI_3Cl_3$ compounds, respectively. The lone pairs cause huge variations in the Sn(Ge)-X octahedral bond lengths and also enhance the hybridization interaction between sn-*s* and X-*p* orbitals, leading to a highly dispersed band (~2.5 eV) at the valence band maximum, giving rise to light holes. The broad bandgap tuning with the closer lattice parameters can enable the fabrication of functionally graded material with varying halide constituents leading to tandem solar cells that can absorb a broad range of the solar spectrum. These findings may provide insights and propel further research into the progress of the environmental-friendly solar materials.

Declaration of Competing Interest

The authors declare that they have no known competing financial interests or personal relationships that could have appeared to influence the work reported in this paper.

References

Becker, M., Klüner, T., Wark, M., 2017. Formation of hybrid ABX 3 perovskite compounds for solar cell application: first-principles calculations of effective ionic radii and determination of tolerance factors. J. Dalton Trans. 46, 3500–3509.

Chen, M., Ju, M.-G., Garces, H.F., Carl, A.D., Ono, L.K., Hawash, Z., Zhang, Y., Shen, T., Qi, Y., Grimm, R.L., Pacifici, D., Zeng, X.C., Zhou, Y., Padture, N.P., 2019. Highly stable and efficient all-inorganic lead-free perovskite solar cells with native-oxide passivation. Nat. Commun. 10 (1).

Fabini, D.H., Seshadri, R., Kanatzidis, M.G., 2020. The underappreciated lone pair in halide perovskites underpins their unusual properties. J. MRS Bull. Kanatzidis. 45 (6), 467–477.

Feng, J., Xiao, B., 2014. Effective masses and electronic and optical properties of nontoxic MASnX3 (X= Cl, Br, and I) perovskite structures as solar cell absorber: a theoretical study using HSE06. J. Phys. Chem. 118, 19655–19660.

Feynman, R.P., 1939. Forces in molecules. J. Phys. Rev. 56 (4), 340–343.

Gidlow, D.A., 2004. Lead toxicity. J. Occupat. Med. 54, 76–81.

Gonze, X., Amadon, B., Anglade, P.-M., Beuken, J.-M., Bottin, F., Boulanger, P., Bruneval, F., Caliste, D., Caracas, R., Côté, M., Deutsch, T., Genovese, L., Ghosez, P. h., Giantomassi, M., Goedecker, S., Hamann, D.R., Hermet, P., Jollet, F., Jomard, G., Leroux, S., Mancini, M., Mazevet, S., Oliveira, M.J.T., Onida, G., Pouillon, Y., Rangel, T., Rignanese, G.-M., Sangalli, D., Shaltaf, R., Torrent, M., Verstraete, M.J., Zerah, G., Zwanziger, J.W., 2009. ABINIT: First-principles approach to material and nanosystem properties. Comput. Phys. Commun. 180 (12), 2582–2615.

Grancini, G., Roldán-Carmona, C., Zimmermann, I., Mosconi, E., Lee, X., Martineau, D., Narbey, S., Oswald, F., De Angelis, F., Graetzel, M., Nazeeruddin, M.K., 2017. One-Year stable perovskite solar cells by 2D/3D interface engineering. Nature Commun. Graetzel. 8 (1).

Hamann, D.R., 2013. Optimized norm-conserving Vanderbilt pseudopotentials. J. Phys. Rev. 88.

Hieulle, J., Wang, X., Stecker, C., Son, D.-Y., Qiu, L., Ohmann, R., Ono, L.K., Mugarza, A., Yan, Y., Qi, Y., 2019. Unraveling the Impact of Halide Mixing on Perovskite Stability. J. Am. Chem. Soc. 141 (8), 3515–3523.

Hu, Y., Hutter, E.M., Rieder, P., Grill, I., Hanisch, J., Aygüler, M.F., Hufnagel, A.G., Handloser, M., Bein, T., Hartschuh, A., Tvingstedt, K., Dyakonov, V., Baumann, A., Savenije, T.J., Petrus, M.L., Docampo, P., 2018. Understanding the Role of Cesium and Rubidium Additives in Perovskite Solar Cells: Trap States, Charge Transport, and Recombination. Adv. Energy Mater. 8 (16), 1703057.

Huckaba, A.J., Lee, Y., Xia, R., Paek, S., Bassetto, V.C., Oveisi, E., Lesch, A., Kinge, S., Dyson, P.J., Girault, H., Nazeeruddin, M.K., 2019. Inkjet-Printed Mesoporous TiO 2 and Perovskite Layers for High Efficiency Perovskite Solar Cells. Energy Technol. 7 (2), 317–324.

Karlsson, M., Yi, Z., Reichert, S., Luo, X., Lin, W., Zhang, Z., Bao, C., Zhang, R., Bai, S., Zheng, G., Teng, P., 2021. Mixed halide perovskites for spectrally stable and high-efficiency blue light-emitting diodes. J. Nat. Commun. 12, 1–10.

Knight, A.J., Borchert, J., Oliver, R.D., Patel, J.B., Radaelli, P.G., Snaith, H.J., Johnston, M.B., Herz, L.M., 2021. Halide segregation in mixed-halide perovskites: influence of A-site cations. J ACS energy letters 6, 799–808.

Liu, D., Liang, L., Sa, R., 2021. First-principles calculations of structural, electronic, and optical properties of double perovskites Cs2Sn1-xBxI6 (B= Si, Ge; x= 0, 0.25, 0.50, 0.75, 1). J. Chem. Phys. 542, 111075.

Moghadamgohari, Z.R., Heidariramsheh, M., Taghavinia, N., Mohammadpour, R., Rasuli, R., 2022. Cu2ZnSnS4 as a hole-transport layer in triple-cation perovskite solar cells: Current density versus layer thickness. Ceramics Int. Rasuli. 48, 711–719.

Momma, K., Izumi, F., 2011. VESTA 3 for three-dimensional visualization of crystal, volumetric and morphology data. J. Appl. Crystall. 44, 1272–1276.

Patrick, C.E., Jacobsen, K.W., Kristian, S., 2015. Anharmonic stabilization and band gap renormalization in the perovskite CsSnI 3. Phys. Rev. B Thygesen. 92, 201205.

Perdew, J.P., Burke, K., Ernzerhof, M., 1996. Generalized gradient approximation made simple. Phys. Rev. Lett. Ernzerhof. 77 (18), 3865–3868.

Raja, D.B., Sundaram, K.S., Vidya, R., 2020. First principle study on hybrid organic-inorganic perovskite ASnBr 3 (A= Formamidinium, Dimethylammonium and Azetidinium). Sol. Energy 207, 1348–1355.

Ravindran, P., Vidya, R., Kjekshus, A., Fjellvåg, H., 2006. Theoretical investigation of magnetoelectric behavior in Bi FeO_3. Phys. Rev. B Eriksson 74.

Smiles, M.J., Skelton, J.M., Shiel, H., Jones, L.A., Swallow, J.E., Edwards, H.J., Murgatroyd, P.A., Featherstone, T.J., Thakur, P.K., Lee, T.L., Dhanak, V.R., 2021. Ge 4s 2 lone pairs and band alignments in GeS and GeSe for photovoltaics. J. Mater. Chem. 9, 22440–22452.

Spek, A.L.J., 2003. Single-crystal structure validation with the program PLATON. J. Appl. Crystallogr. 36, 7–13.

Stoumpos, C.C., Kanatzidis, M.G., 2015. The Renaissance of Halide Perovskites and Their Evolution as Emerging Semiconductors. Acc. Chem. Res. 48 (10), 2791–2802.

Tien, C.H., Chen, L.C., Lee, K.L., 2021. Ultra-thin and high transparent Cu2ZnSnSe4/NiOx double-layered inorganic hole-transporting layer for inverted structure CH3NH3PbI3 perovskite solar cells. J. Alloys Compd. 873.

Zarabinia, N., Rasuli, R., 2021. Electronic and optical properties of halide double-perovskites under strain: a density functional study. J. Energy Sources Part A: Recovery Utilization Environ. Effects 43, 2443–2455.

Zhao, D., Wang, C., Song, Z., Yu, Y., Chen, C., Zhao, X., Zhu, K., Yan, Y., 2018. Four-Terminal All-Perovskite Tandem Solar Cells Achieving Power Conversion Efficiencies Exceeding 23%. ACS Energy Lett. 3 (2), 305–306.

Zhou, Q., Ma, W., Zhang, Z., Liu, Y., Zhang, H., Mao, Y., 2021. Double-layered hole transport material of CuInS2/Spiro for highly efficient and stable perovskite solar cells. Org. Electron. 96, 106249.